

Fully automated 3D segmentation of dopamine transporter SPECT images using an estimation-based approach

Ziping Liu^a, Hae Sol Moon^a, Richard Laforest^b, Joel S. Perlmutter^{b,c}, Scott A. Norris^{b,c}, Abhinav K. Jha^{a,b,*}

^a*Department of Biomedical Engineering, Washington University in St. Louis, St. Louis, MO, USA*

^b*Department of Radiology, Washington University School of Medicine, St. Louis, MO, USA*

^c*Department of Neurology, Washington University School of Medicine, St. Louis, MO, USA*

Abstract

Quantitative measures of uptake in the caudate, putamen, and globus pallidus in dopamine transporter (DaT) brain SPECT have potential as biomarkers for the severity of Parkinson disease. Reliable quantification of this uptake requires accurate segmentation of these regions. However, segmentation is challenging in DaT SPECT due to partial-volume effects, system noise, physiological variability, and the small size of these regions. To address these challenges, we propose an estimation-based approach to segmentation. This approach estimates the posterior mean of the fractional volume occupied by caudate, putamen, and globus pallidus within each voxel of a 3D SPECT image. The estimate is obtained by minimizing a cost function based on the binary cross-entropy loss between the true and estimated fractional volumes over a population of SPECT images, where the distribution of the true fractional volumes is obtained from magnetic resonance images from clinical populations. The proposed method accounts for both the sources of partial-volume effects in SPECT, namely the limited system resolution and tissue-fraction effects. The method was implemented using a deep-learning-based approach and evaluated using realistic clinically guided SPECT simulation studies, where the ground-truth properties of caudate, putamen, and GP were known. The method significantly outperformed all other considered segmentation methods, including a U-net-based method, and yielded accurate segmentation with dice similarity coefficients of ~ 0.80 for all regions. Further, the method was relatively insensitive to the changes in voxel size. Overall, the results demonstrate the efficacy of the proposed method to yield accurate fully automated segmentation of caudate, putamen, and globus pallidus in 3D DaT-SPECT images.

Keywords: Parkinsonian syndromes, single-photon emission computed tomography, estimation, segmentation, partial volume effects, tissue fraction effects

*Corresponding author

Email address: a.jha@wustl.edu (Abhinav K. Jha)

1. Introduction

Parkinson disease (PD) is the second-most common neurodegenerative disease. The disease is relentlessly progressive and will affect 12 million people worldwide by 2040 (Fahn and Sulzer, 2004; Dorsey et al., 2018; Dorsey and Bloem, 2018). Dopamine transporter (DaT) single-photon emission computed tomography (SPECT) measures pre-synaptic dopaminergic neurons that are known to degenerate in patients with PD. Of the various DaT-based ligands (Emamzadeh and Surguchov, 2018), DaTscan (Ioflupane I-123 injection) is FDA approved to assist with the evaluation of adult patients with suspected parkinsonian syndromes (I13, 2011). For this clinical application, DaT-SPECT images typically are analyzed visually by trained readers. However, this is error-prone and suffers from intra- and inter-reader variability (Augimeri et al., 2016). To address this issue, several studies are investigating whether quantitative uptakes in striatal regions, i.e. the caudate and putamen, provide more useful clinical information (Joling et al., 2017). Further, shape (Staff et al., 2009; Prashanth et al., 2016) and texture (Martinez-Murcia et al., 2014; Augimeri et al., 2016) analyses of striatal regions are also being explored to enhance the clinical applications of DaT SPECT. Conducting these quantification, shape- and texture-analysis studies requires reliable segmentation of caudate and putamen from DaT-SPECT images.

Further, the greatest unmet therapeutic need in PD is for disease-modifying therapies (Lang and Espay, 2018). While no such therapies have been identified, several are being investigated (Lang and Espay, 2018; AlDakheel et al., 2014; Elkouzi et al., 2019). Biomarkers that accurately reflect disease severity are critical for these studies and the need is pressing (McGhee et al., 2013). Most studies on developing such biomarkers have focused on the striatal uptake, but such measures may correlate with severity only early in the disease (Perlmutter and Norris, 2014; Saari et al., 2017; Honkanen et al., 2019; Karimi et al., 2013). Thus, there remains an important need for improved biomarkers that can measure severity throughout the range of the disease. Measurements in globus pallidus (GP) may play a key role. Several post-mortem studies demonstrated altered DaT uptake in GP (Ciliax et al., 1999; Porritt et al., 2005). Clinical studies have observed correlations between DaT reduction in GP and resting tremor severity (Helmich et al., 2011). In addition, small-sized studies suggest that degeneration of nigrostriatal dopamine neurons in early PD is compensated in part by increased DaT uptake in GP that is lost in more advanced stages of disease (Whone et al., 2003). The observations have led to the hypothesis that the plasticity of the nigropallidal pathway helps maintain a more normal pattern of pallidal output to ventral thalamus and motor cortex in early PD. Further, the loss of this pathway in advanced disease may be a pivotal step in disease progression. Similar findings were reported in parkinsonism secondary to occupational manganese toxicity (Emamzadeh and Surguchov, 2018). Thus, investigating DaT uptake in GP may help provide a measure of PD severity. DaT-SPECT studies provide a mechanism to study these effects *in vivo*. However, this requires the availability of tools to segment the

GP in SPECT images, and such tools are currently not available. Thus, there is an important need to develop such tools.

Segmentation in SPECT is challenging due to limited system resolution, system noise, and physiological variability in patient populations (Badiavas et al., 2011; Dewaraja et al., 2001). In addition, the caudate, putamen, and GP are in proximity to each other. The limited system resolution in SPECT blurs the boundaries of these regions, thus making the segmentation task challenging. In fact, GP is visually almost impossible to demarcate from SPECT images, and to the best of our knowledge, there are no validated automated or semi-automated tools to segment the GP. Another challenge is the small size of these regions. GP is ~ 3 cubic centimeter (cc), while caudate and putamen are ~ 10 cc. Segmentation is typically performed manually by trained readers, but that is expensive, tedious, time-consuming, and suffers from intra- and inter-reader variability, especially due to the poor resolution in SPECT (Jha et al., 2017a). To address this issue, several semi-automated SPECT segmentation methods have been proposed, such as those based on thresholding (Long et al., 1992; Tsujimoto et al., 2018), edge detection (Long et al., 1992), region growing (Slomka et al., 1995), and clustering (Mignotte et al., 2001). However, our studies showed that these methods typically segmented the caudate, putamen, and GP as highly overlapped regions in DaT-SPECT images. Further, these methods also yield large variabilities in DaT-SPECT-derived metrics, and thus may have limited clinical utility (Matesan et al., 2018). Thus, there remains an important need for improved methods to segment DaT-SPECT images, and in particular, methods that can segment the GP.

To address this need, we recognize that a major barrier to segmenting the caudate, putamen, and GP is the lack of clear boundaries between these regions in SPECT images. This barrier arises due to partial-volume effects (PVEs) in the reconstructed images (Soret et al., 2007). PVEs have two sources, namely the limited system resolution and tissue-fraction effects (TFEs) (Rousset et al., 2007). The resolution of clinical brain SPECT systems is typically ~ 8 mm, and the resolution in reconstructed images can be ~ 12 mm (Stam et al., 2018; Council et al., 1996). Thus, structures such as caudate, putamen, and GP that are close to each other, are heavily affected by this limited resolution. Further, due to the reconstruction of image over finite-sized voxel grids, voxels on the boundary of two regions likely contain both the regions. While this is generally an issue in medical imaging, the effect is more prominent in SPECT due to the larger voxel sizes.

Conventional segmentation methods are typically designed to perform segmentation through voxel-wise classification, i.e. each image voxel is assigned as exclusively belonging to one region. Thus, these methods are inherently limited in accounting for TFEs. Probabilistic techniques such as fuzzy segmentation methods (Chen et al., 2019) and probabilistic atlas-based segmentation methods (Lee and Lee, 2005), can provide a probabilistic estimate of each image voxel belonging to a certain region. However, this probabilistic estimate is only a measure of uncer-

tainty in classification and thus has no relation to the TFEs. Conventional deep-learning (DL)-based segmentation methods (Leung et al., 2020; Lin et al., 2020) are designed and trained on the task of classifying each image voxel as belonging to one region. While these methods can also output probabilistic estimates for each image voxel, the estimates again only infer classification uncertainty and do not relate to the TFEs.

To account for both the sources of PVEs, Liu et al. (2021) recently proposed an estimation-based segmentation technique, in the context of segmenting tumors in oncological positron emission tomography (PET) images. This technique is designed to estimate the fractional volume that a tumor occupies within each voxel of a PET image. Through this strategy, TFEs can be explicitly modeled. In this manuscript, we propose to advance this estimation-based technique in the context of segmenting the caudate, putamen, and GP in 3-D DaT-SPECT images and while using information from other imaging modalities. Our proposed method is a Bayesian approach, and as shown later, requires a distribution of the fractional volumes that caudate, putamen, and GP occupy within each image voxel. This distribution is obtained from clinical T1-weighted magnetic resonance (MR) images, where these regions are visible separately and can be delineated. The method then uses this distribution to estimate the posterior mean of the fractional volumes of caudate, putamen, and GP in DaT-SPECT images. We first provide the theory behind the proposed method.

2. Methods

2.1. Theory

2.1.1. Problem formulation

Consider a patient injected with a DaT-based tracer such as 123-Ioflupane. Let $f(\mathbf{r})$ describe the DaT-tracer distribution within the brain, where $\mathbf{r} = (x, y, z)$ is a 3-D vector denoting spatial coordinates. Consider a SPECT system that images this patient and yields sinogram data. This data is then input to a reconstruction algorithm, yielding a reconstructed image $\hat{\mathbf{f}}$ consisting of M voxels. Denote the process of obtaining the reconstructed image from the original tracer distribution by the operator $\Theta : \mathbb{L}_2(\mathbb{R}^3) \rightarrow \mathbb{E}^M$. As outlined in Sec. 1, our objective is to design an approach that estimates the fractional volume occupied by the k^{th} region of left and right caudate, putamen, and GP in each voxel of the reconstructed image $\hat{\mathbf{f}}$. Using this approach, we are able to explicitly model TFEs while performing segmentation.

Let the support of the k^{th} region be given by $\phi_k(\mathbf{r})$, i.e.

$$\phi_k(\mathbf{r}) = \begin{cases} 1, & \text{if region } k \text{ occupies location } \mathbf{r}. \\ 0, & \text{otherwise.} \end{cases} \quad (1)$$

Next, define the voxel function $\psi_m(\mathbf{r})$ as

$$\psi_m(\mathbf{r}) = \begin{cases} 1, & \text{if } \mathbf{r} \text{ lies within the } m^{\text{th}} \text{ voxel in the DaT-SPECT image.} \\ 0, & \text{otherwise.} \end{cases} \quad (2)$$

Let V denote the total volume of each voxel. The fractional volume occupied by the k^{th} region in the m^{th} voxel in the SPECT image, denoted by $v_{\text{ideal},k,m}$, is given by

$$v_{\text{ideal},k,m} = \frac{1}{V} \int d^3\mathbf{r} \phi_k(\mathbf{r})\psi_m(\mathbf{r}). \quad (3)$$

Estimating the fractional volumes within each voxel thus requires estimating the values of $\phi_k(\mathbf{r})$ from $\hat{\mathbf{f}}$. This is an ill-posed problem due to the null functions of the Θ operator. One way to alleviate this ill-posedness is to incorporate prior distribution of $\phi_k(\mathbf{r})$. To obtain this distribution, we benefit from the availability of existing MR-image populations, which can provide the distribution of $\phi_k(\mathbf{r})$ at relatively higher resolution. More specifically, the boundaries of caudate, putamen, and GP are distinguishable on MR images due to the higher resolution of MRI. Thus, the acquired MR images can be segmented to obtain a distribution of the support of these regions.

Denote the MR image by an N -dimensional vector \mathbf{f}_{MR} , where $N > M$. The voxel function for this image is denoted as $\psi_n^{MR}(\mathbf{r})$. Consider that this image has been segmented into K distinct regions. For each region, we define an N -dimensional vector ϕ_k^{MR} , which denotes the support of that region. The elements of this vector are defined as follows:

$$\phi_{k,i}^{MR} = \begin{cases} 1, & \text{if voxel } i \text{ in the MR image is assigned to region } k. \\ 0, & \text{otherwise.} \end{cases} \quad (4)$$

Consider a patient population where the MR and SPECT images are co-registered. Thus, from the MR images in this population, we can obtain a discrete version of the support of the k^{th} region as defined in Eq. (1), at a higher resolution than the SPECT images. The ground-truth fractional volume of k^{th} region in the m^{th} voxel of the SPECT image can thus be calculated as follows:

$$v_{k,m} = \frac{1}{V} \sum_{n=1}^N \phi_{k,n}^{MR} \int d^3\mathbf{r} \psi_n^{MR}(\mathbf{r})\psi_m(\mathbf{r}), \quad (5)$$

where the integral computes the volume that the n^{th} voxel in the MR image occupies within the m^{th} voxel of the SPECT image. We frame our problem as the task of estimating these true fractional volumes $\{v_{k,m}, k = 1, 2, \dots, K, m = 1, 2, \dots, M\}$ from the SPECT images.

2.1.2. Estimation technique

Let the estimate of $v_{k,m}$ be defined as $\hat{v}_{k,m}$. Denote the vector $\{v_{k,m}, m = 1, 2, \dots, M\}$ by \mathbf{v}_k , and the estimate of \mathbf{v}_k by $\hat{\mathbf{v}}_k$. To compute $\hat{\mathbf{v}}_k$ from the reconstructed SPECT image $\hat{\mathbf{f}}$, we first need to define a cost function. In this problem, values of $v_{k,m}$ and $\hat{v}_{k,m}$ are constrained to lie between 0 and 1. Using binary cross-entropy (BCE) loss function allows us to automatically incorporate this constraint on the range of these values (Creswell et al., 2017). Thus, the BCE loss, denoted by $l_{\text{BCE}}(v_{k,m}, \hat{v}_{k,m})$ and given by the equation below, is chosen as the basis of our cost function:

$$l_{\text{BCE}}(v_{k,m}, \hat{v}_{k,m}) = -v_{k,m} \log(\hat{v}_{k,m}) - (1 - v_{k,m}) \log(1 - \hat{v}_{k,m}). \quad (6)$$

The cost function, denoted by $C(\mathbf{v}_k, \hat{\mathbf{v}}_k)$, is defined to minimize the negative of aggregate BCE loss between $v_{k,m}$ and $\hat{v}_{k,m}$ over all M voxels, averaged over the ensemble of true values $v_{k,m}$ and the noise $\hat{\mathbf{f}}$ in the imaging process. The cost function is then given by:

$$C(\mathbf{v}_k, \hat{\mathbf{v}}_k) = - \sum_{m=1}^M \int d^M \hat{\mathbf{f}} \int dv_{k,m} \text{pr}(\hat{\mathbf{f}}, v_{k,m}) l_{\text{BCE}}(v_{k,m}, \hat{v}_{k,m}). \quad (7)$$

Using conditional probability to expand $\text{pr}(\hat{\mathbf{f}}, v_{k,m})$ and replacing the expression from Eq. (6) in Eq. (7), we obtain

$$\begin{aligned} C(\mathbf{v}_k, \hat{\mathbf{v}}_k) &= \sum_{m=1}^M \int d^M \hat{\mathbf{f}} \text{pr}(\hat{\mathbf{f}}) \int dv_{k,m} \text{pr}(v_{k,m} | \hat{\mathbf{f}}) \left[v_{k,m} \log(\hat{v}_{k,m}) + (1 - v_{k,m}) \log(1 - \hat{v}_{k,m}) \right] \\ &= \sum_{m=1}^M \int d^M \hat{\mathbf{f}} \text{pr}(\hat{\mathbf{f}}) \int dv_{k,m} \text{pr}(v_{k,m} | \hat{\mathbf{f}}) \left[\log(1 - \hat{v}_{k,m}) + v_{k,m} \{ \log(\hat{v}_{k,m}) - \log(1 - \hat{v}_{k,m}) \} \right]. \end{aligned} \quad (8)$$

Since $\int dv_{k,m} \text{pr}(v_{k,m} | \hat{\mathbf{f}}) = 1$, Eq. (8) becomes

$$C(\mathbf{v}_k, \hat{\mathbf{v}}_k) = \sum_{m=1}^M \int d^M \hat{\mathbf{f}} \text{pr}(\hat{\mathbf{f}}) \left[\log(1 - \hat{v}_{k,m}) + \{ \log(\hat{v}_{k,m}) - \log(1 - \hat{v}_{k,m}) \} \int dv_{k,m} \text{pr}(v_{k,m} | \hat{\mathbf{f}}) v_{k,m} \right]. \quad (9)$$

Our objective is to find the value of $\hat{v}_{k,m}$ that minimizes this cost function. This is the point at which the derivative of the cost function with respect to $\hat{v}_{k,m}$ is 0. Since the term $\text{pr}(\hat{\mathbf{f}})$ is always non-negative, the cost function is minimized by setting

$$\frac{\partial}{\partial \hat{v}_{k,m}} \left[\log(1 - \hat{v}_{k,m}) + \{ \log(\hat{v}_{k,m}) - \log(1 - \hat{v}_{k,m}) \} \int dv_{k,m} \text{pr}(v_{k,m} | \hat{\mathbf{f}}) v_{k,m} \right] = 0. \quad (10)$$

The solution is given by

$$\hat{v}_{k,m}^* = \int dv_{k,m} \text{pr}(v_{k,m} | \hat{\mathbf{f}}) v_{k,m}. \quad (11)$$

This is simply the posterior mean estimate of $v_{k,m}$. Thus, by developing an optimization procedure that minimizes the cost function defined in Eq. (9), we obtain an estimator that yields the posterior mean estimate of the ground-truth fractional volume occupied by the left and right caudate, putamen, and GP in each voxel of the SPECT image. Note that the same estimator is obtained when the ensemble mean squared error is defined as the cost function. Thus, this estimator also yields the lowest mean squared error among all estimators. We next describe our optimization procedure.

2.2. Implementation of the proposed method

To minimize the cost function given by Eq. (9) requires sampling from the posterior distribution $\text{pr}(v_{k,m}|\hat{\mathbf{f}})$. This is challenging since this distribution is high dimensional and an analytical form for the distribution is unavailable. To address this challenge, the proposed method was implemented using a DL-based approach (Fig. 1). In the training phase, the network was input a population of 3-D SPECT images and the corresponding ground-truth fractional volumes occupied by caudate, putamen, and GP, i.e. \mathbf{v}_k for each image, as described in Sec. 2.1.1. The network was trained by minimizing the cost function defined in Eq. (9) to yield a posterior mean estimate of the fractional volumes occupied by these regions within each image voxel.

The network design for the proposed method is similar to other networks that are designed for estimation-based tasks, such as those for image denoising (Creswell et al., 2017) and reconstruction (Nath et al., 2020). Briefly, the network consists of an encoder and decoder, each containing cascades of convolutional layers. The encoder extracts local spatial features from the input SPECT image and the decoder maps the extracted features to the fractional volumes. In the final layer, the network outputs the fractional volumes occupied by left and right caudate, putamen, and GP in each voxel of the input SPECT image. To improve training performance, several features were adopted in the network design. Following each convolutional layer, an activation function of leaky rectified linear unit (ReLU) was applied to accelerate the convergence speed (Xu et al., 2015). Dropout was used as a regularization strategy to prevent overfitting (Srivastava et al., 2014). In addition, skip connections with element-wise addition were applied between the output of layers in the encoder and decoder to stabilize network training (Mao et al., 2016). Further, instead of conducting slice-by-slice segmentation or patch-based training (Kamnitsas et al., 2017), the network was designed in fully 3-D to provide the maximal amount of global contextual information per patient image. The detail of the network architecture is given in the appendix (Table A1).

The network architecture and training were implemented in Python 3.6.9 and Keras 2.2.4. For effective training performance on 3-D images, experiments were performed on a Red Hat Enterprise Linux 7.7 operating system with two 24 GB NVIDIA Titan RTX graphics processing unit cards.

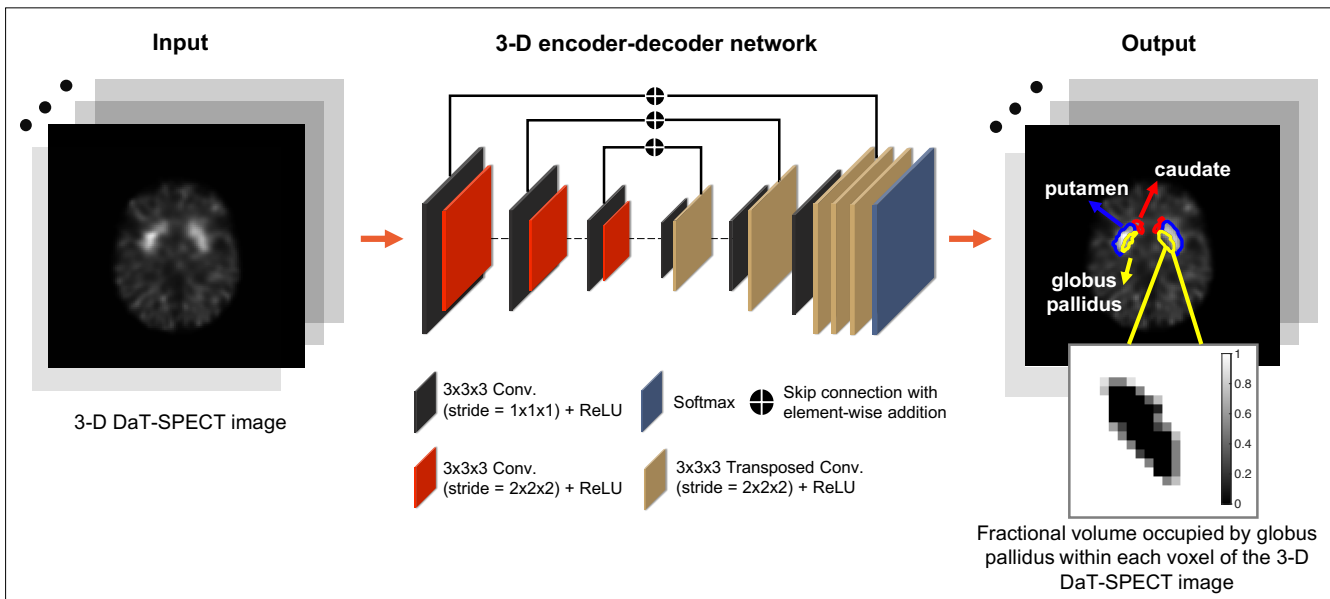


Figure 1: Illustration of the implementation of the proposed method. The network, when input a 3-D DaT-SPECT image, outputs the estimated fractional volumes occupied by left and right caudate, putamen and GP within each voxel of the image.

3. Evaluation

Evaluation of the proposed method using clinical data requires access to DaT-SPECT images, where the ground-truth fractional volumes of caudate, putamen, and GP are known. One approach to conducting such a study is to have expert readers delineate these regions. However, manual delineations are not guaranteed to be accurate due to PVEs in SPECT. In fact, GP is almost impossible to delineate manually on the DaT-SPECT images. Further, the boundaries between caudate and putamen are unclear. Even more importantly, accounting for TFEs while performing manual delineations is challenging. Finally, manual delineations are well known to suffer from intra- and inter-reader variability (Augimeri et al., 2016). All these factors make manual delineations a limited measure of ground truth. This issue of lack of ground truth when evaluating methods for quantitative imaging is often addressed by conducting realistic simulation studies (Du et al., 2005; Ouyang et al., 2006; Du and Frey, 2009; Jin et al., 2013; Jha et al., 2016). Realistic simulations provide a mechanism to evaluate imaging methods with known ground truth, model imaging physics, and account for patient-population variability. Thus, we developed a clinically guided and realistic simulation-based approach to evaluate the proposed method. In this approach, clinical MR images were used to generate clinically realistic SPECT images by accurately modeling the tracer distributions and SPECT imaging physics.

Note that while this approach required simulation of SPECT system, the ground-truth distribution of the fractional volumes of caudate, putamen, and GP was not simulated and was obtained directly from clinical studies. Further, a clinical SPECT system and a clinical acquisition protocol was simulated. Additionally, the system was simulated using well-validated Monte Carlo (MC)-based methods, as we describe below. The goal was to make our study highly realistic and clinically relevant. Below, we describe the process to objectively evaluate the proposed method using this simulation-based approach.

3.1. Generating realistic SPECT images

A total of 580 T1-weighted MR images of cognitively healthy patients from the Open Access Series of Imaging Studies-3 (LaMontagne et al., 2019) were used. Caudate, putamen, and GP for both left and right hemispheres were segmented from these images using the Freesurfer software (Fischl, 2012). The segmentations were performed in Montreal Neurological Institute (MNI) space and then transformed back into each patient’s native space, yielding 580 anatomical brain templates. These templates were of $256 \times 256 \times 256$ voxels, with the voxel size of $1 \text{ mm} \times 1 \text{ mm} \times 1 \text{ mm}$. Next, clinically realistic distributions of the DaT specific binding ratios of caudate, putamen, and GP were defined. These distributions were defined as normal distributions with the mean and standard deviation values obtained from clinical data (Son et al., 2016), as presented in Table 1. For each anatomical brain template, these distributions were sampled to determine the DaT uptake in different regions. This process ensured clinically realistic variability of the regional DaT uptakes in the simulated patient populations. At the end of this process, we had a digital phantom population of 580 patients with anatomical templates directly obtained from clinical data and tracer distributions guided by clinical data.

Region	Mean specific binding ratio	Standard deviation
Left/right caudate	3.283	0.802
Left/right putamen	2.920	0.458
Left/right globus pallidus	1.856	0.398

Table 1: Mean and standard deviation of the specific binding ratio of caudate, putamen, and globus pallidus based on Son et al. (2016). The occipital region was chosen as the reference region.

These ground-truth tracer distributions were then used to generate realistic DaTscan SPECT images. A SPECT system with acquisition parameters similar to the GE Discovery 670 scanner (GE Healthcare, Haifa, Israel) was simulated. The acquisition modeled a DaTscan SPECT protocol with ^{123}I -Ioflupane tracer and a low-energy high-resolution (LEHR) collimator. Projection data were generated using SIMIND, a well-validated MC-based simulation

method (Ljungberg et al., 2012). This simulation modeled all relevant image-degrading processes in SPECT, including photon attenuation and scatter, the finite extent of the collimator with thickness of 3.5 cm, the finite energy resolution of 9.8%, and the intrinsic spatial resolution of 0.39 cm at 159 keV of the detector. Following the Society of Nuclear Medicine Practice guideline for DaTscan SPECT (Djang et al., 2012), 120 projection views for full 360° coverage of the head were acquired. The number of total detected counts was scaled to clinically realistic value of 2 million counts, to which Poisson noise was added. The noisy projection data were then reconstructed using an iterative 3-D ordered subset expectation maximization (OSEM)-based algorithm with 4 iterations and 8 subsets that compensated for attenuation, scatter, and detector response. The overall procedure to generate the SPECT images is summarized in Fig. 2.

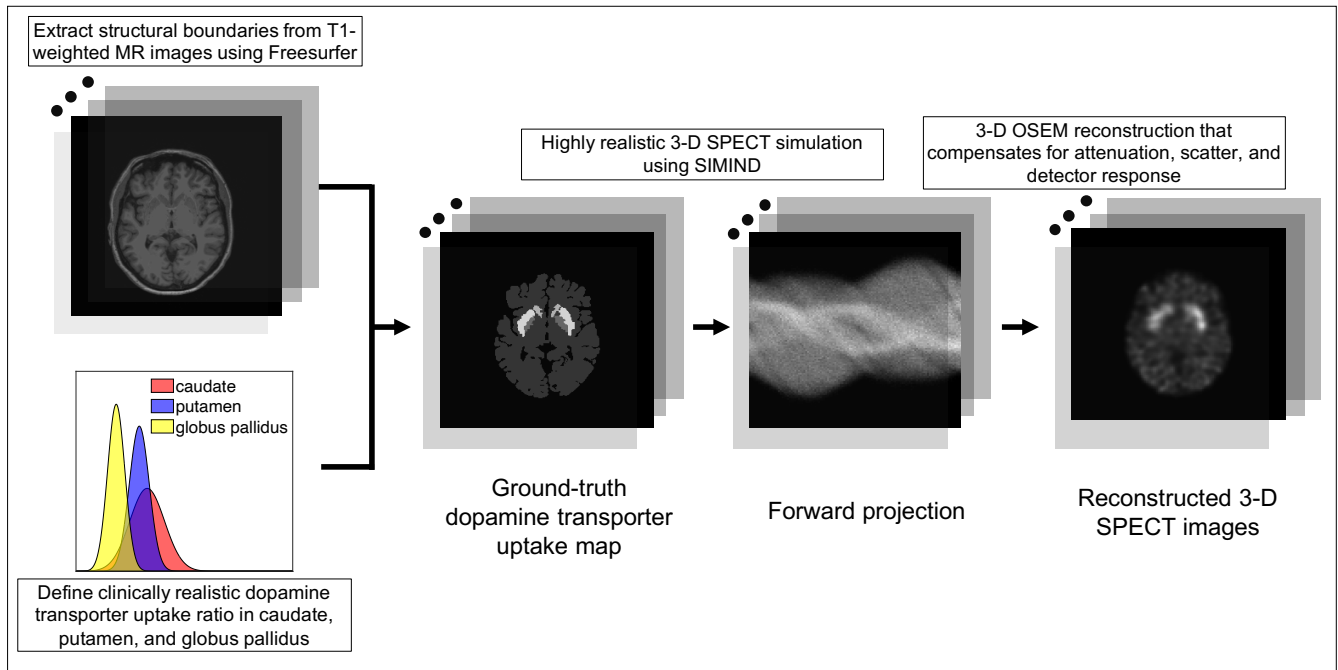


Figure 2: Strategy to generate highly realistic simulated SPECT images. A digital phantom population of 580 patients were generated with anatomical templates obtained from existing MR images and tracer distributions guided by clinical data. The digital phantoms were input to SIMIND Monte Carlo simulation software to obtain projection data. The projection data were then fed into a 3-D OSEM-based reconstruction algorithm to generate reconstructed SPECT images.

3.2. Training strategy

Following the simulation procedure described above, a total of 580 reconstructed 3-D DaTscan SPECT images were generated. Of the 580 SPECT images, 480 images were used for network training and validation using 5-fold cross validation. The remaining 100 completely independent images were reserved for evaluating the performance of the proposed method.

Our training strategy was designed specifically for the goal of explicitly modeling TFEs, as described in Sec. 2.1.1. Thus, the ground truth was defined as the fractional volumes occupied by caudate, putamen, and GP within each voxel of a SPECT image. The inputs to the network were the SPECT image and the corresponding true fractional volumes within each voxel of this image. The true fractional volumes were obtained using the Freesurfer-defined segmentations on corresponding MR images. These segmentations provided the high-resolution support of each region, i.e. ϕ_k^{MR} as defined in Sec. 2.1.1. From this support, using Eq. (5), we obtained the ground-truth fractional volumes. The network was then trained to yield a posterior mean estimate of the true fractional volumes by minimizing the cost function $C(\mathbf{v}_k, \hat{\mathbf{v}}_k)$ given by Eq. (9).

3.3. Evaluation strategy

3.3.1. Evaluation metrics

The proposed method was quantitatively evaluated on the 100 independent test images, using metrics that evaluated spatial overlap and shape similarity. In the category of spatial-overlap metrics, we used the dice similarity coefficient (DSC) and jaccard similarity coefficient (JSC). For each voxel in a SPECT image, the method yields continuous-valued fractional volumes. Thus, the DSC and JSC were defined as in Taha and Hanbury (2015) to evaluate segmentation methods that yield such non-binary outputs. Higher values of DSC and JSC lead to the inference of more accurate segmentation performance. In addition, the shape similarity between the true and estimated segmentations was quantified using the Hausdorff distance (HD) (Huttenlocher et al., 1993). For this purpose, a topographic map was constructed for each of the left and right caudate, putamen, and GP, using the corresponding estimated fractional volumes. The ground-truth topographic map of each region was also constructed using the true fractional volumes. From the topographic map of each region, the set of points with the value of fractional volume equal to 0.5 was defined as the boundary. The coordinates of points along the boundary were then used to compute the HD. Lower values of HD lead to the inference of higher accuracy in boundary delineation. All metrics were reported as mean values with 95% confidence intervals (CIs). A paired sample t -test with p -value < 0.01 was performed to assess statistical significance.

3.3.2. Evaluating accuracy and comparing to other segmentation methods

The proposed method was quantitatively compared to several commonly used segmentation methods, on the basis of DSC, JSC, and HD. Common methods for segmenting nuclear-medicine images can be classified as those based on thresholding, boundary detection, stochastic modeling, and learning (Foster et al., 2014). In our study, 40% SUV-max thresholding (King et al., 1991), Snakes (Kass et al., 1988), Markov random fields-Gaussian mixture model (MRF-GMM), and a U-net-based method (Leung et al., 2020) were chosen in each of these categories. Note that the U-net-based method, similar to conventional DL-based methods, was designed and trained on the task of classifying each voxel as exclusively belonging to one region. The 40% SUV-max, Snakes, and MRF-GMM methods required manual inputs in the form of a seed voxel and/or an initial boundary estimate. The proposed and U-net-based method instead did not require any manual input and were fully automated.

3.3.3. Evaluating sensitivity to voxel sizes

To conduct this evaluation, we generated two sets of 580 simulated SPECT images, with the voxel size of $2\text{ mm} \times 2\text{ mm} \times 2\text{ mm}$ and $4\text{ mm} \times 4\text{ mm} \times 4\text{ mm}$, respectively. The simulation procedure for each set of images followed the description in Sec. 3.1. Zoom factor (field of view) was adjusted to allow for reconstruction with different voxel sizes. For each voxel size, the network was trained and cross-validated on 480 of the 580 images, following the training strategy in Sec. 3.2. The trained network was then evaluated on the remaining 100 independent test images. The performance of the proposed method was quantified on the basis of DSC, JSC, and HD.

4. Results

4.1. Evaluating accuracy and comparing to other segmentation methods

Quantitatively, for all the left and right caudate, putamen, and GP, the proposed method significantly outperformed ($p < 0.01$) the 40% SUV-max, Snakes, and MRF-GMM, on the basis of DSC, JSC, and HD (Fig. 3, Table A2 and A3 in the appendix). Further, the proposed method yielded DSC of ~ 0.80 for all regions, indicating an accurate segmentation performance (Zijdenbos et al., 1994).

Qualitatively, Fig. 4 shows the comparison between the ground-truth boundaries of caudate, putamen, and GP and the boundaries estimated using the proposed method. The boundaries were obtained following the procedure described in Sec. 3.3.1. We observe that the proposed method yielded reliable boundaries of all regions and provided a close match to the ground-truth boundaries.

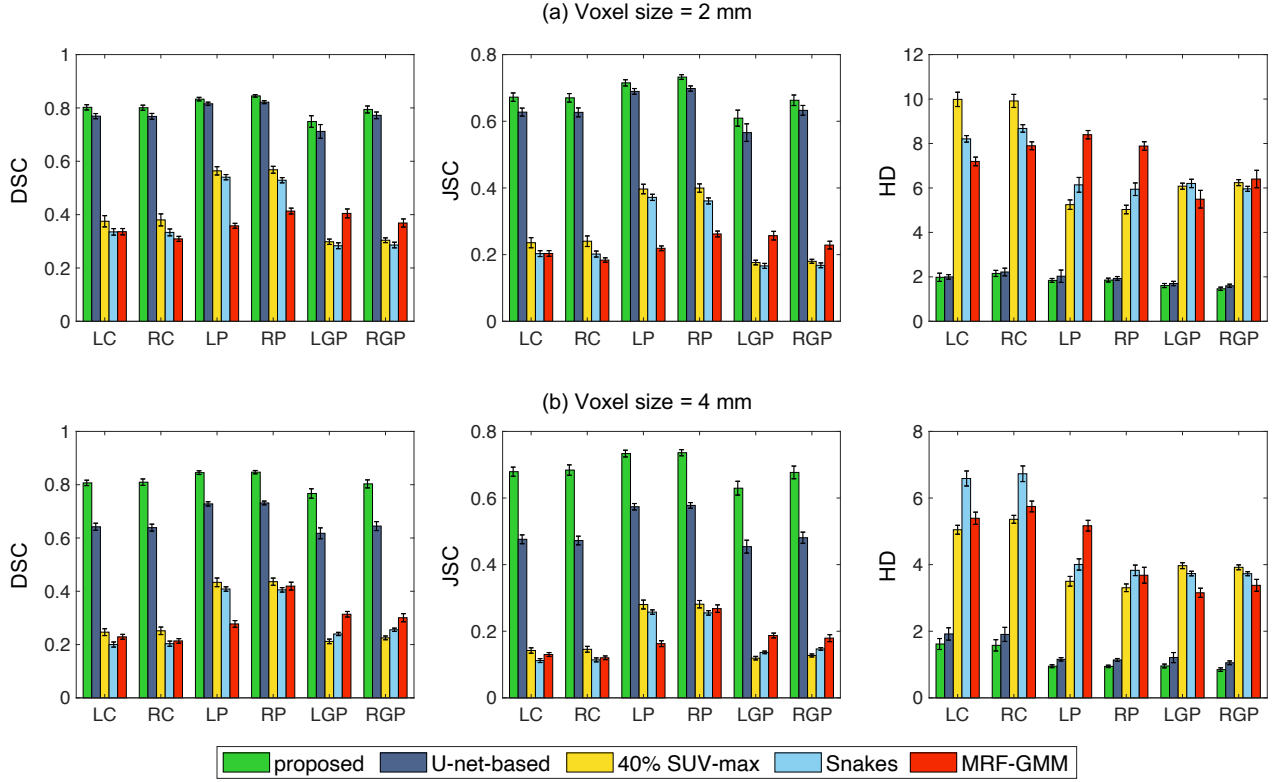


Figure 3: Quantitative comparison of the segmentation performance between the proposed method and other considered methods, on the basis of dice similarity coefficient, jaccard similarity coefficient, and Hausdorff distance, for SPECT images with voxel size of (a) 2 mm and (b) 4 mm, respectively. (LC/RC: left/right caudate; LP/RP: left/right putamen; LGP/RGP: left/right globus pallidus)

Additionally, we observe in Fig. 5 that the 40% SUV-max, Snakes, and MRF-GMM all segmented the caudate, putamen, and GP as highly overlapped regions. In contrast, the proposed method was able to segment these regions separately and closely matched the ground truth.

4.2. Evaluating sensitivity to voxel sizes

Fig. 3 shows that the proposed method yielded accurate segmentation performance for both 2 mm and 4 mm voxel sizes, and significantly outperformed the U-net-based method on the basis of DSC and JSC. Note that the difference in segmentation performance between the proposed and U-net-based method decreased from the voxel size of 4 mm to 2 mm. This was because TFEs were less dominant in the reconstructed images with smaller voxel size.

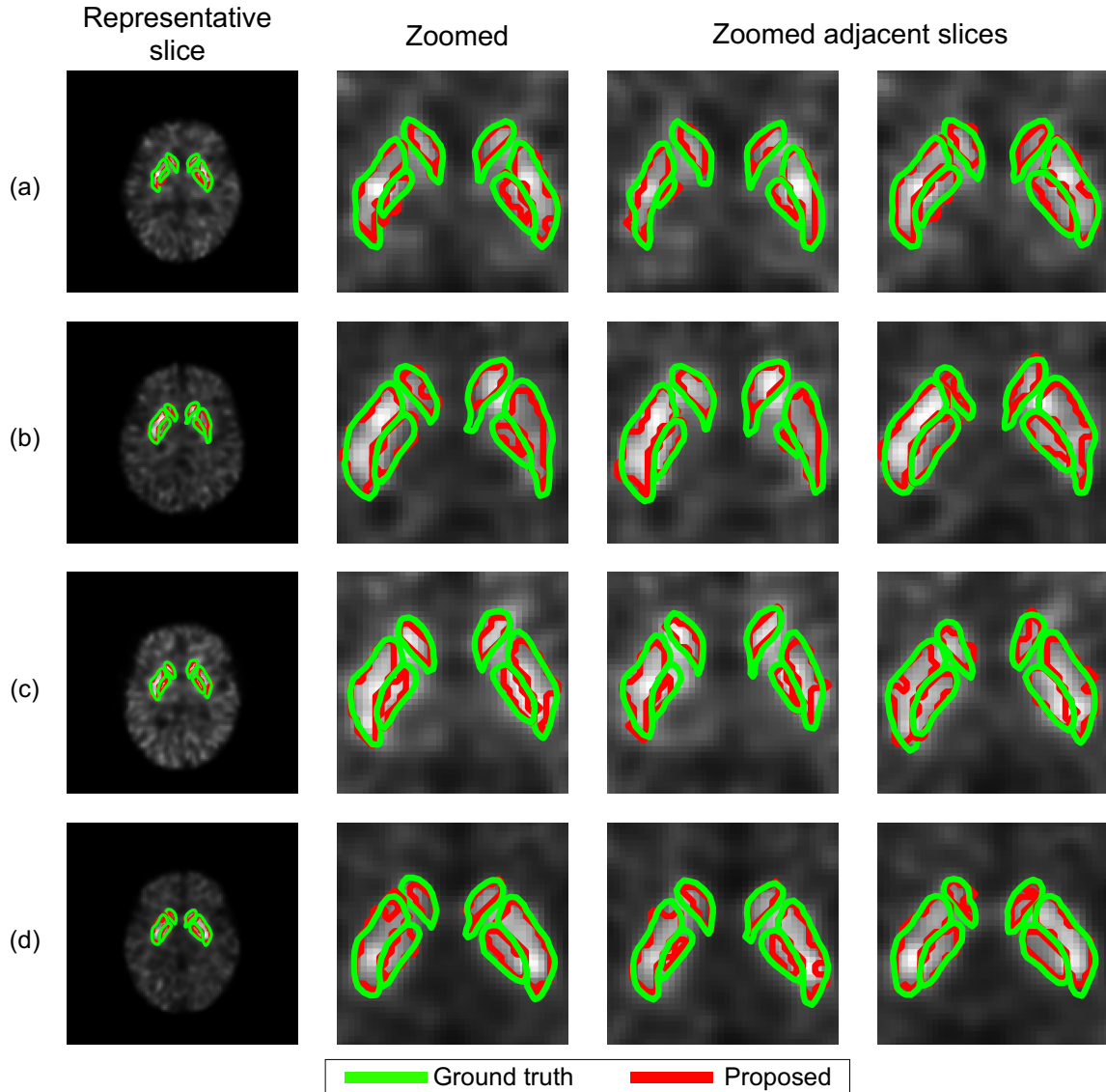


Figure 4: Qualitative evaluation of the proposed method for four representative simulated patients. The true boundaries (green) of caudate, putamen, and globus pallidus and the boundaries estimated using the proposed method (red) were compared. The shown reconstructed SPECT images were with voxel size of 2 mm.

For the proposed method, DSC and JSC remained relatively unchanged on varying the voxel size from 2 mm to 4 mm, indicating that the method was relatively insensitive to changes in voxel size. This insensitivity was due to the capability of the method to explicitly model the TFEs. In contrast, the U-net-based method yielded limited

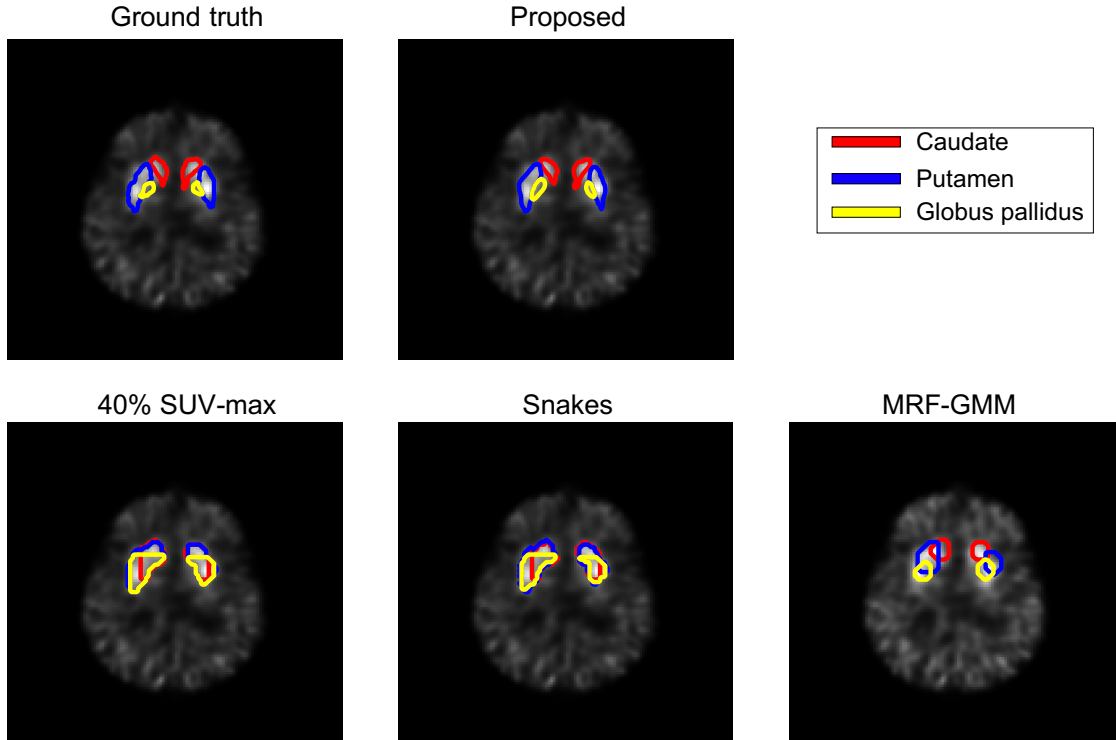


Figure 5: Qualitative comparison between the true and estimated boundaries of left and right caudate, putamen, and globus pallidus using conventional semi-automated segmentation methods. Boundaries yielded by the proposed method are also shown for comparison. The shown reconstructed SPECT images were with voxel size of 2 mm.

performance for the 4 mm voxel size, demonstrating that not modeling TFEs has a tangibly adverse impact on segmentation performance.

5. Discussion

We proposed an estimation-based approach to fully automated 3-D DaT-SPECT segmentation. The proposed method accounts for PVEs, and in particular, TFEs, while performing segmentation. Our results demonstrate the efficacy of the method to accurately segment caudate, putamen, and GP in DaT-SPECT images. In particular, ability to segment the small-sized GP is distinctive as this region is visually almost impossible to demarcate and currently, to the best of our knowledge, no validated tools are available to segment this region in DaT-SPECT images. This is clinically important as delineating GP presents an opportunity to rigorously evaluate pallidal

uptake as a biomarker for measuring the severity of PD. This also opens up a new and important research frontier on analyzing the functional characteristics of the GP in patients with PD. In addition, the method accurately segmented the caudate and putamen in DaT-SPECT images. This provides a tool to evaluate quantitative features, including the shape and texture analysis of these regions, to determine whether differences exist in different forms of parkinsonism. These studies may lead to new biomarkers for measuring the severity of PD and possibly for differential diagnosis.

We observe from Fig. 3 that the proposed method yielded accurate segmentation for all regions and significantly outperformed the other considered segmentation methods, including a U-net-based method (Leung et al., 2020). While the U-net-based and proposed method both learn anatomical variability and PVEs due to the limited system resolution, the proposed method additionally accounts for PVEs due to TFEs that arise from the larger voxel size in reconstructed SPECT images. Thus, the proposed method yielded significantly improved performance compared to segmentation methods that do not account for TFEs. This explains the larger difference in the values of DSC and JSC between the proposed and U-net-based method when the reconstructed images have the larger 4 mm voxel size. The higher accuracy of the proposed method for 4 mm voxel size is especially important as many clinical DaT-SPECT scans are conducted with 4 mm voxel size (Djang et al., 2012). Additionally, we observe in Fig. 3 that a change in the voxel size from 2 mm to 4 mm did not impact the performance of the proposed method. However, the DSC of the U-net-based method decreased by more than 10%. This provides evidence that the proposed method is relatively robust to changes in voxel size and provides distinct and quantitatively measurable advantages to existing methods.

Application of the proposed method to segment a DaT-SPECT image in a clinical or research setting does not require the image of the patient from any other modalities such as MRI. This is an important advantage of our method. Another class of methods to segment striatal regions in DaT-SPECT images uses MR images of the same patient acquired from a different scanner (Rahmim et al., 2016). These methods have not been evaluated for segmenting GP. Further, these methods require SPECT and MR images of the patient, which may not be available. One mechanism to obtain such images in future may be from SPECT/MR systems (Hutton et al., 2018), but these are currently not available clinically. The proposed method, by virtue of having no such requirement, can segment the DaT-SPECT image of a patient even when the corresponding MR image is not available. This advantage may facilitate the wider adoption of this method. However, the proposed method does require SPECT and MR images during the training phase. This could be obtained from databases such as Parkinson Progression Biomarker Initiative (PPMI). However, further studies will be needed to evaluate whether training with such a database may be generalizable to scanners. Another option is to use simulation-based approaches for pre-training the network,

followed by training with a small number of registered SPECT and MR images. A similar approach was suggested in Leung et al. (2020) and was observed to significantly reduce the number of training images. Investigating the performance of this and other transfer-learning-based approaches to training is an important area of future research.

There are some limitations in our study. First, the proposed method was evaluated using simulation studies. The simulations used clinical MR images as anatomical templates so that the distribution of the true fractional volumes was obtained directly from clinical imaging data. Further, the simulations accurately modeled the tracer distributions and SPECT imaging physics. However, the simulations may not have modeled all aspects of patient physiology and system instrumentation. Evaluation using physical-phantom and patient studies can help address these limitations by modeling all aspects of system instrumentation and modeling patient physiology accurately, respectively. Validation with patient studies requires a gold standard and that is not available for these types of images. To address this challenge, no-gold-standard (NGS) evaluation techniques have been developed (Kupinski et al., 2002; Jha et al., 2012, 2016, 2017b; Liu et al., 2020). These techniques would provide an approach to clinically evaluate the proposed method.

Another limitation is that we focused on segmenting the caudate, putamen, and GP in DaT-SPECT images and considered the rest of brain as background. However, post-mortem and PET-based studies have identified DaT uptake in other brain regions such as nucleus accumbens and substantia nigra (Sun et al., 2012; Brown et al., 2013). Further, the GP can itself be separated into two parts, namely the internal and external GP. It remains to be determined how these two parts may contribute independently to PD progression. Results from this study motivate extending the proposed method to segment these regions. Finally, in our simulation studies, we assume that the uptake within the various regions is uniform. However, the tracer uptake within the putamen may be heterogeneous in patients with PD. Modeling this heterogeneity and evaluating the performance of the proposed method in the presence of this heterogeneity are important research areas.

6. Conclusion

In this manuscript, we proposed an estimation-based fully automated method to segment the caudate, putamen, and globus pallidus in 3-D DaT-SPECT images. The method accounts for both the sources of partial-volume effects in SPECT, namely system-generated blur and tissue-fraction effects. Essentially, the method estimates the posterior mean of the fractional volume that the different regions occupy within each voxel of a SPECT image, where the prior distribution of the fractional volumes were obtained from existing MR-image populations. Evaluation using realistic clinically guided simulation studies shows that the method accurately segmented the caudate, putamen, and globus pallidus in 3D DaT-SPECT images. The method significantly outperformed all other considered segmentation

methods, including a U-net-based method, by yielding high DSC of ~ 0.80 for all regions. Further, the method was relatively insensitive to changes in voxel size. Overall, the results demonstrate the efficacy of our method in 3-D DaT-SPECT segmentation and motivate further evaluation with physical-phantom and patient studies.

Acknowledgements

This work was supported by the National Institute of Biomedical Imaging and Bioengineering Trailblazer R21 Award (R21-EB024647) and the NVIDIA GPU grant, the American Parkinson Disease Association (APDA), the Greater St. Louis Chapter of the APDA, the Barnes-Jewish Hospital Foundation (Elliot Stein Family Fund), and the Paula & Rodger Riney Fund. The authors also thank the Washington University Center for High Performance Computing for providing computational resources. The center is partially funded by NIH grants 1S10RR022984-01A1 and 1S10OD018091-01.

References

- DaTscan (Ioflupane I 123 Injection) for Intravenous Use, CII Initial U.S. Approval. 2011. URL: https://www.accessdata.fda.gov/drugsatfda_docs/label/2011/0224540rig1s000Lb1.pdf.
- AlDakheel A, Kalia LV, Lang AE. Pathogenesis-targeted, disease-modifying therapies in parkinson disease. *Neurotherapeutics* 2014;11(1):6–23.
- Augimeri A, Cherubini A, Cascini GL, Galea D, Caligiuri ME, Barbagallo G, Arabia G, Quattrone A. CADA—computer-aided DaTSCAN analysis. *EJNMMI Phys* 2016;3(1):4.
- Badiavas K, Molyvda E, Iakovou I, Tsolaki M, Psarrakos K, Karatzas N. SPECT imaging evaluation in movement disorders: far beyond visual assessment. *EJNMMI Phys* 2011;38(4):764–73.
- Brown CA, Karimi MK, Tian L, Flores H, Su Y, Tabbal SD, Loftin SK, Moerlein SM, Perlmutter JS. Validation of midbrain positron emission tomography measures for nigrostriatal neurons in macaques. *Ann Neurol* 2013;74(4):602–10.
- Chen J, Jha AK, Frey EC. Incorporating CT prior information in the robust fuzzy C-means algorithm for QSPECT image segmentation. In: *SPIE Medical Imaging. International Society for Optics and Photonics; volume 10949; 2019. p. 109491W.*
- Ciliax BJ, Drash GW, Staley JK, Haber S, Mobley CJ, Miller GW, Mufson EJ, Mash DC, Levey AI. Immunocytochemical localization of the dopamine transporter in human brain. *J Comp Neurol* 1999;409(1):38–56.
- Council NR, et al. Single Photon Emission Computed Tomography. In: *Mathematics and Physics of Emerging Biomedical Imaging. National Academies Press (US); 1996. .*
- Creswell A, Arulkumaran K, Bharath AA. On denoising autoencoders trained to minimise binary cross-entropy. *arXiv preprint arXiv:170808487* 2017;.
- Dewaraja YK, Ljungberg M, Koral KF. Monte Carlo evaluation of object shape effects in iodine-131 SPECT tumor activity quantification. *Eur J Nucl Med* 2001;28(7):900–6.
- Djang DS, Janssen MJ, Bohnen N, Booij J, Henderson TA, Herholz K, Minoshima S, Rowe CC, Sabri O, Seibyl J, et al. SNM practice guideline for dopamine transporter imaging with 123I-Ioflupane SPECT 1.0. *J Nucl Med* 2012;53(1):154–63.

- Dorsey E, Sherer T, Okun MS, Bloem BR. The emerging evidence of the Parkinson pandemic. *J Parkinsons Dis* 2018;8(s1):S3–8.
- Dorsey ER, Bloem BR. The Parkinson pandemic—a call to action. *JAMA Neurol* 2018;75(1):9–10.
- Du Y, Frey EC. Quantitative evaluation of simultaneous reconstruction with model-based crosstalk compensation for dual-isotope simultaneous acquisition brain SPECT. *Med Phys* 2009;36(6Part1):2021–33.
- Du Y, Tsui BM, Frey EC. Partial volume effect compensation for quantitative brain SPECT imaging. *IEEE Trans Med Imag* 2005;24(8):969–76.
- Elkouzi A, Vedam-Mai V, Eisinger RS, Okun MS. Emerging therapies in Parkinson disease—repurposed drugs and new approaches. *Nat Rev Neurol* 2019;15(4):204–23.
- Emamzadeh FN, Surguchov A. Parkinson’s disease: biomarkers, treatment, and risk factors. *Front Neurosci* 2018;12:612.
- Fahn S, Sulzer D. Neurodegeneration and neuroprotection in Parkinson disease. *NeuroRx* 2004;1(1):139–54.
- Fischl B. Freesurfer. *Neuroimage* 2012;62(2):774–81.
- Foster B, Bagci U, Mansoor A, Xu Z, Mollura DJ. A review on segmentation of positron emission tomography images. *Comp Biol Med* 2014;50:76–96.
- Helmich RC, Janssen MJ, Oyen WJ, Bloem BR, Toni I. Pallidal dysfunction drives a cerebellothalamic circuit into Parkinson tremor. *Ann Neurol* 2011;69(2):269–81.
- Honkanen EA, Saari L, Orte K, Gardberg M, Noponen T, Joutsa J, Kaasinen V. No link between striatal dopaminergic axons and dopamine transporter imaging in parkinson’s disease. *Mov Disord* 2019;34(10):1562–6.
- Huttenlocher DP, Klanderman GA, Rucklidge WJ. Comparing images using the Hausdorff distance. *IEEE Trans Pattern Anal Mach Intell* 1993;15(9):850–63.
- Hutton BF, Occhipinti M, Kuehne A, Máthé D, Kovács N, Waiczies H, Erlandsson K, Salvado D, Carminati M, Montagnani GL, et al. Development of clinical simultaneous SPECT/MRI. *Br J Radiol* 2018;91(1081):20160690.
- Jha A, Rowe S, Du Y, Frey E. An unsupervised semi-automated segmentation technique to delineate tumors and bones in SPECT images of patients with bone metastasis. *J Nucl Med* 2017a;58(supplement 1):613–.

- Jha AK, Caffo B, Frey EC. A no-gold-standard technique for objective assessment of quantitative nuclear-medicine imaging methods. *Phys Med Biol* 2016;61(7):2780.
- Jha AK, Kupinski MA, Rodriguez JJ, Stephen RM, Stopeck AT. Task-based evaluation of segmentation algorithms for diffusion-weighted MRI without using a gold standard. *Phys Med Biol* 2012;57(13):4425.
- Jha AK, Mena E, Caffo BS, Ashrafinia S, Rahmim A, Frey EC, Subramaniam RM. Practical no-gold-standard evaluation framework for quantitative imaging methods: application to lesion segmentation in positron emission tomography. *J Med Imag* 2017b;4(1):011011.
- Jin X, Mulnix T, Gallezot JD, Carson RE. Evaluation of motion correction methods in human brain PET imaging—A simulation study based on human motion data. *Medical physics* 2013;40(10):102503.
- Joling M, Vriend C, Van den Heuvel OA, Raijmakers PG, Jones PA, Berendse HW, Booij J. Analysis of extrastriatal 123I-FP-CIT binding contributes to the differential diagnosis of Parkinsonian diseases. *J Nucl Med* 2017;58(7):1117–23.
- Kamnitsas K, Ledig C, Newcombe VF, Simpson JP, Kane AD, Menon DK, Rueckert D, Glocker B. Efficient multi-scale 3D CNN with fully connected CRF for accurate brain lesion segmentation. *Med Image Anal* 2017;36:61–78.
- Karimi M, Tian L, Brown CA, Flores HP, Loftin SK, Videen TO, Moerlein SM, Perlmutter JS. Validation of nigrostriatal positron emission tomography measures: critical limits. *Ann Neurol* 2013;73(3):390–6.
- Kass M, Witkin A, Terzopoulos D. Snakes: Active contour models. *Int J Comp Vision* 1988;1(4):321–31.
- King MA, Long DT, Brill AB. SPECT volume quantitation: influence of spatial resolution, source size and shape, and voxel size. *Med Phys* 1991;18(5):1016–24.
- Kupinski MA, Hoppin JW, Clarkson E, Barrett HH, Kastis GA. Estimation in medical imaging without a gold standard. *Acad Radiol* 2002;9(3):290–7.
- LaMontagne PJ, Benzinger TL, Morris JC, Keefe S, Hornbeck R, Xiong C, Grant E, Hassenstab J, Moulder K, Vlassenko A, et al. Oasis-3: longitudinal neuroimaging, clinical, and cognitive dataset for normal aging and alzheimer disease. *medRxiv* 2019;.
- Lang AE, Espay AJ. Disease modification in parkinson’s disease: current approaches, challenges, and future considerations. *Mov Disord* 2018;33(5):660–77.

- Lee JS, Lee DS. Analysis of functional brain images using population-based probabilistic atlas. *Current Medical Imaging* 2005;1(1):81–7.
- Leung KH, Marashdeh W, Wray R, Ashrafinia S, Pomper MG, Rahmim A, Jha AK. A physics-guided modular deep-learning based automated framework for tumor segmentation in PET. *Phys Med Biol* 2020;.
- Lin Q, Luo M, Gao R, Li T, Man Z, Cao Y, Wang H. Deep learning based automatic segmentation of metastasis hotspots in thorax bone SPECT images. *PLOS One* 2020;15(12):e0243253.
- Liu J, Liu Z, Moon HS, Mhlanga J, Jha A. A no-gold-standard technique for objective evaluation of quantitative nuclear-medicine imaging methods in the presence of correlated noise. *J Nucl Med* 2020;61(supplement 1):523–.
- Liu Z, Mhlanga JC, Laforest R, Derenoncourt PR, Siegel BA, Jha AK. A Bayesian approach to tissue-fraction estimation for oncological PET segmentation. *Phys Med Biol* 2021;66(12):124002.
- Ljungberg M, Strand S, King M. The simind monte carlo program. *Monte Carlo calculation in nuclear medicine: Applications in diagnostic imaging* 2012;:145–63.
- Long DT, King MA, Sheehan J. Comparative evaluation of image segmentation methods for volume quantitation in SPECT. *Med Phys* 1992;19(2):483–9.
- Mao XJ, Shen C, Yang YB. Image restoration using very deep convolutional encoder-decoder networks with symmetric skip connections. *arXiv preprint arXiv:160309056* 2016;.
- Martinez-Murcia F, Górriz J, Ramírez J, Moreno-Caballero M, Gómez-Río M, Initiative PPM. Parametrization of textural patterns in 123I-ioflupane imaging for the automatic detection of Parkinsonism. *Med Phys* 2014;41(1):012502.
- Matesan M, Gaddikeri S, Longfellow K, Miyaoka R, Elojeimy S, Elman S, Hu SC, Minoshima S, Lewis D. I-123 DaTscan SPECT Brain Imaging in Parkinsonian Syndromes: Utility of the Putamen-to-Caudate Ratio. *J Neuroimaging* 2018;28(6):629–34.
- McGhee DJ, Royle PL, Thompson PA, Wright DE, Zajicek JP, Counsell CE. A systematic review of biomarkers for disease progression in parkinson’s disease. *BMC Neurol* 2013;13(1):35.
- Mignotte M, Meunier J, Soucy J, Janicki C. Segmentation and classification of brain SPECT images using 3D Markov random field and density mixture estimations. In: *Proc. 5th World Multi-Conf. Systemics, Cybernetics and Informatics, Concepts and Applications of Systemics and Informatics*. Citeseer; volume 10; 2001. p. 239–44.

- Nath V, Pathak SK, Schilling KG, Schneider W, Landman BA. Deep learning estimation of multi-tissue constrained spherical deconvolution with limited single shell DW-MRI. In: SPIE Medical Imaging. International Society for Optics and Photonics; volume 11313; 2020. p. 113130S.
- Ouyang J, El Fakhri G, Moore SC, Kijewski MF. Fast Monte Carlo Simulation Based Joint Iterative Reconstruction for Simultaneous $^{99m}\text{Tc}/^{123}\text{I}$ Brain SPECT Imaging. In: 2006 IEEE Nuclear Science Symposium Conference Record. IEEE; volume 4; 2006. p. 2251–6.
- Perlmutter JS, Norris SA. Neuroimaging biomarkers for Parkinson’s disease: Facts and fantasy. *Ann Neurol* 2014;76(6):769–83.
- Porritt M, Stanic D, Finkelstein D, Batchelor P, Lockhart S, Hughes A, Kalnins R, Howells D. Dopaminergic innervation of the human striatum in Parkinson’s disease. *Mov Disord* 2005;20(7):810–8.
- Prashanth R, Roy SD, Mandal PK, Ghosh S. High-accuracy classification of Parkinson’s disease through shape analysis and surface fitting in ^{123}I -Ioflupane SPECT imaging. *IEEE J Biomed Health Inform* 2016;21(3):794–802.
- Rahmim A, Salimpour Y, Jain S, Blinder SA, Klyuzhin IS, Smith GS, Mari Z, Sossi V. Application of texture analysis to DAT SPECT imaging: relationship to clinical assessments. *NeuroImage: Clinical* 2016;12:e1–9.
- Rousset O, Rahmim A, Alavi A, Zaidi H. Partial volume correction strategies in PET. *PET Clin* 2007;2(2):235–49.
- Saari L, Kivinen K, Gardberg M, Joutsa J, Nojonen T, Kaasinen V. Dopamine transporter imaging does not predict the number of nigral neurons in parkinson disease. *Neurology* 2017;88(15):1461–7.
- Slomka PJ, Hurwitz GA, Clement GS, Stephenson J. Three-dimensional demarcation of perfusion zones corresponding to specific coronary arteries: application for automated interpretation of myocardial SPECT. *J Nucl Med* 1995;36(11):2120–6.
- Son SJ, Kim M, Park H. Imaging analysis of parkinson’s disease patients using spect and tractography. *Scientific reports* 2016;6:38070.
- Soret M, Bacharach SL, Buvat I. Partial-volume effect in PET tumor imaging. *J Nucl, Med* 2007;48(6):932–45.
- Srivastava N, Hinton G, Krizhevsky A, Sutskever I, Salakhutdinov R. Dropout: a simple way to prevent neural networks from overfitting. *J Mach Learn Res* 2014;15(1):1929–58.

- Staff RT, Ahearn TS, Wilson K, Counsell CE, Taylor K, Caslake R, Davidson JE, Gemmell HG, Murray AD. Shape analysis of ^{123}I -N- ω -fluoropropyl-2- β -carbomethoxy-3 β -(4-iodophenyl) nortropane single-photon emission computed tomography images in the assessment of patients with Parkinsonian syndromes. *Nucl Med Comm* 2009;30(3):194–201.
- Stam M, Verwer E, Booij J, Adriaanse S, de Bruin C, de Wit T. Performance evaluation of a novel brain-dedicated SPECT system. *EJNMMI Phys* 2018;5(1):1–14.
- Sun J, Xu J, Cairns NJ, Perlmutter JS, Mach RH. Dopamine D1, D2, D3 receptors, vesicular monoamine transporter type-2 (VMAT2) and dopamine transporter (DAT) densities in aged human brain. *PloS One* 2012;7(11):e49483.
- Taha AA, Hanbury A. Metrics for evaluating 3D medical image segmentation: analysis, selection, and tool. *BMC Med Imag* 2015;15(1):29.
- Tsujimoto M, Teramoto A, Ota S, Toyama H, Fujita H. Automated segmentation and detection of increased uptake regions in bone scintigraphy using SPECT/CT images. *Ann Nucl Med* 2018;32(3):182–90.
- Whone AL, Moore RY, Piccini PP, Brooks DJ. Plasticity of the nigropallidal pathway in Parkinson’s disease. *Ann Neurol* 2003;53(2):206–13.
- Xu B, Wang N, Chen T, Li M. Empirical evaluation of rectified activations in convolutional network. arXiv preprint arXiv:150500853 2015;.
- Zijdenbos AP, Dawant BM, Margolin RA, Palmer AC. Morphometric analysis of white matter lesions in MR images: method and validation. *IEEE Trans Med Imag* 1994;13(4):716–24.

Appendix

Detailed architecture of the encoder-decoder network designed for the proposed method is given in Table A1.

Quantification results of the proposed method and other considered segmentation methods are provided in Table A2 and Table A3.

Table A1: Detailed architecture parameters. (Conv.: convolutional)

	Layer Type	# of filters	Filter size	Stride	Input Size	Output Size
Layer 1	Conv.	32	$3 \times 3 \times 3$	$1 \times 1 \times 1$	$128 \times 128 \times 128 \times 1$	$128 \times 128 \times 128 \times 32$
Layer 2	Conv.	32	$3 \times 3 \times 3$	$2 \times 2 \times 2$	$128 \times 128 \times 128 \times 32$	$64 \times 64 \times 64 \times 32$
Layer 3	Conv.	64	$3 \times 3 \times 3$	$1 \times 1 \times 1$	$64 \times 64 \times 64 \times 32$	$64 \times 64 \times 64 \times 64$
Layer 4	Conv.	64	$3 \times 3 \times 3$	$2 \times 2 \times 2$	$64 \times 64 \times 64 \times 64$	$32 \times 32 \times 32 \times 64$
Layer 5	Conv.	128	$3 \times 3 \times 3$	$1 \times 1 \times 1$	$32 \times 32 \times 32 \times 64$	$32 \times 32 \times 32 \times 128$
Layer 6	Conv.	128	$3 \times 3 \times 3$	$2 \times 2 \times 2$	$32 \times 32 \times 32 \times 128$	$16 \times 16 \times 16 \times 128$
Layer 7	Conv.	256	$3 \times 3 \times 3$	$1 \times 1 \times 1$	$16 \times 16 \times 16 \times 128$	$16 \times 16 \times 16 \times 256$
Layer 8	Transposed Conv.	128	$3 \times 3 \times 3$	$2 \times 2 \times 2$	$16 \times 16 \times 16 \times 256$	$32 \times 32 \times 32 \times 128$
Layer 9	Add Layer 5	-	-	-	$32 \times 32 \times 32 \times 128$	$32 \times 32 \times 32 \times 128$
Layer 10	Conv.	128	$3 \times 3 \times 3$	$1 \times 1 \times 1$	$32 \times 32 \times 32 \times 128$	$32 \times 32 \times 32 \times 128$
Layer 11	Transposed Conv.	64	$3 \times 3 \times 3$	$2 \times 2 \times 2$	$32 \times 32 \times 32 \times 128$	$64 \times 64 \times 64 \times 64$
Layer 12	Add Layer 3	-	-	-	$64 \times 64 \times 64 \times 64$	$64 \times 64 \times 64 \times 64$
Layer 13	Conv.	64	$3 \times 3 \times 3$	$1 \times 1 \times 1$	$64 \times 64 \times 64 \times 64$	$64 \times 64 \times 64 \times 64$
Layer 14	Transposed Conv.	32	$3 \times 3 \times 3$	$2 \times 2 \times 2$	$64 \times 64 \times 64 \times 64$	$128 \times 128 \times 128 \times 32$
Layer 15	Add Layer 1	-	-	-	$128 \times 128 \times 128 \times 32$	$128 \times 128 \times 128 \times 32$
Layer 16	Conv.	32	$3 \times 3 \times 3$	$1 \times 1 \times 1$	$128 \times 128 \times 128 \times 32$	$128 \times 128 \times 128 \times 32$
Layer 17	Conv.	7	$3 \times 3 \times 3$	$1 \times 1 \times 1$	$128 \times 128 \times 128 \times 32$	$128 \times 128 \times 128 \times 7$
Output	Softmax	-	-	-	$128 \times 128 \times 128 \times 7$	$128 \times 128 \times 128 \times 7$

Table A2: Quantitative comparison between the proposed method and other segmentation methods on the basis of dice similarity coefficient, jaccard similarity coefficient and hausdorff distance, for reconstructed images with voxel size of 2 mm. (LC/RC: left/right caudate; LP/RP: left/right putamen; LGP/RGP: left/right globus pallidus)

	Proposed	U-net-based	40% SUV-max	Snakes	MRF-GMM
DSC (LC)	0.8(0.79, 0.81)	0.77(0.76, 0.78)	0.38(0.35, 0.4)	0.34(0.32, 0.35)	0.34(0.32, 0.35)
DSC (RC)	0.8(0.79, 0.81)	0.77(0.76, 0.78)	0.38(0.36, 0.4)	0.33(0.32, 0.35)	0.31(0.3, 0.32)
DSC (LP)	0.83(0.83, 0.84)	0.82(0.81, 0.82)	0.56(0.55, 0.58)	0.54(0.53, 0.55)	0.36(0.35, 0.37)
DSC (RP)	0.85(0.84, 0.85)	0.82(0.82, 0.83)	0.57(0.56, 0.58)	0.53(0.52, 0.54)	0.41(0.4, 0.42)
DSC (LGP)	0.75(0.73, 0.77)	0.71(0.69, 0.74)	0.3(0.29, 0.31)	0.28(0.27, 0.29)	0.4(0.39, 0.42)
DSC (RGP)	0.79(0.78, 0.81)	0.77(0.76, 0.78)	0.3(0.3, 0.31)	0.29(0.28, 0.3)	0.37(0.35, 0.38)
JSC (LC)	0.67(0.66, 0.68)	0.63(0.62, 0.64)	0.24(0.22, 0.25)	0.2(0.19, 0.21)	0.2(0.19, 0.21)
JSC (RC)	0.67(0.66, 0.68)	0.63(0.61, 0.64)	0.24(0.22, 0.26)	0.2(0.19, 0.21)	0.18(0.18, 0.19)
JSC (LP)	0.72(0.71, 0.72)	0.69(0.68, 0.7)	0.4(0.38, 0.41)	0.37(0.36, 0.38)	0.22(0.21, 0.23)
JSC (RP)	0.73(0.73, 0.74)	0.7(0.69, 0.71)	0.4(0.39, 0.41)	0.36(0.35, 0.37)	0.26(0.25, 0.27)
JSC (LGP)	0.61(0.59, 0.63)	0.57(0.54, 0.59)	0.18(0.17, 0.18)	0.17(0.16, 0.17)	0.26(0.24, 0.27)
JSC (RGP)	0.66(0.65, 0.68)	0.63(0.62, 0.65)	0.18(0.17, 0.19)	0.17(0.16, 0.18)	0.23(0.22, 0.24)
HD (LC)	1.98(1.8, 2.17)	2(1.9, 2.1)	9.99(9.66, 10.3)	8.21(8.06, 8.36)	7.19(7, 7.39)
HD (RC)	2.15(2.02, 2.29)	2.22(2.05, 2.39)	9.91(9.62, 10.2)	8.68(8.51, 8.85)	7.9(7.72, 8.07)
HD (LP)	1.84(1.76, 1.93)	2.03(1.75, 2.31)	5.25(5.04, 5.46)	6.14(5.81, 6.47)	8.4(8.21, 8.58)
HD (RP)	1.86(1.77, 1.94)	1.93(1.84, 2.02)	5.03(4.84, 5.22)	5.94(5.66, 6.23)	7.89(7.69, 8.08)
HD (LGP)	1.61(1.52, 1.7)	1.7(1.61, 1.8)	6.08(5.94, 6.22)	6.2(6.01, 6.39)	5.49(5.1, 5.89)
HD (RGP)	1.46(1.39, 1.54)	1.6(1.53, 1.67)	6.24(6.1, 6.37)	5.96(5.85, 6.07)	6.4(6.01, 6.79)

Table A3: Quantitative comparison between the proposed method and other segmentation methods on the basis of dice similarity coefficient, jaccard similarity coefficient and hausdorff distance, for reconstructed images with voxel size of 4 mm. (LC/RC: left/right caudate; LP/RP: left/right putamen; LGP/RGP: left/right globus pallidus)

	Proposed	U-net-based	40% SUV-max	Snakes	MRF-GMM
DSC (LC)	0.81(0.8, 0.82)	0.64(0.63, 0.66)	0.25(0.23, 0.26)	0.2(0.19, 0.21)	0.23(0.22, 0.24)
DSC (RC)	0.81(0.8, 0.82)	0.64(0.63, 0.65)	0.25(0.24, 0.27)	0.2(0.19, 0.21)	0.21(0.21, 0.22)
DSC (LP)	0.85(0.84, 0.85)	0.73(0.72, 0.74)	0.43(0.42, 0.45)	0.41(0.4, 0.42)	0.28(0.26, 0.29)
DSC (RP)	0.85(0.84, 0.85)	0.73(0.72, 0.74)	0.44(0.42, 0.45)	0.41(0.4, 0.41)	0.42(0.4, 0.43)
DSC (LGP)	0.77(0.75, 0.78)	0.62(0.6, 0.64)	0.21(0.2, 0.22)	0.24(0.23, 0.25)	0.31(0.3, 0.32)
DSC (RGP)	0.8(0.79, 0.82)	0.64(0.63, 0.66)	0.23(0.22, 0.23)	0.26(0.25, 0.26)	0.3(0.29, 0.32)
JSC (LC)	0.68(0.67, 0.69)	0.48(0.46, 0.49)	0.14(0.13, 0.15)	0.11(0.11, 0.12)	0.13(0.12, 0.14)
JSC (RC)	0.68(0.67, 0.7)	0.47(0.46, 0.49)	0.15(0.14, 0.15)	0.11(0.11, 0.12)	0.12(0.11, 0.13)
JSC (LP)	0.73(0.72, 0.74)	0.57(0.56, 0.58)	0.28(0.27, 0.29)	0.26(0.25, 0.26)	0.16(0.15, 0.17)
JSC (RP)	0.74(0.73, 0.75)	0.58(0.57, 0.59)	0.28(0.27, 0.29)	0.26(0.25, 0.26)	0.27(0.26, 0.28)
JSC (LGP)	0.63(0.61, 0.65)	0.45(0.43, 0.47)	0.12(0.11, 0.12)	0.14(0.13, 0.14)	0.19(0.18, 0.19)
JSC (RGP)	0.68(0.66, 0.7)	0.48(0.46, 0.5)	0.13(0.12, 0.13)	0.15(0.14, 0.15)	0.18(0.17, 0.19)
HD (LC)	1.62(1.45, 1.78)	1.92(1.73, 2.1)	5.05(4.91, 5.18)	6.59(6.36, 6.81)	5.39(5.21, 5.58)
HD (RC)	1.58(1.41, 1.75)	1.9(1.69, 2.12)	5.36(5.24, 5.48)	6.73(6.49, 6.96)	5.75(5.58, 5.91)
HD (LP)	0.95(0.907, 0.993)	1.16(1.11, 1.21)	3.5(3.35, 3.65)	4(3.84, 4.17)	5.17(5.01, 5.33)
HD (RP)	0.944(0.908, 0.981)	1.14(1.09, 1.18)	3.31(3.19, 3.42)	3.83(3.67, 3.99)	3.68(3.44, 3.92)
HD (LGP)	0.958(0.902, 1.01)	1.21(1.06, 1.36)	3.97(3.88, 4.06)	3.73(3.66, 3.8)	3.16(3.02, 3.29)
HD (RGP)	0.847(0.794, 0.901)	1.05(0.997, 1.11)	3.92(3.85, 3.99)	3.73(3.67, 3.79)	3.38(3.2, 3.56)